JACS
JOURNAL OF THE AMERICAN CHEMICAL SOCIETY
pubs.acs.org/JACS
Article

Ultralong Room-Temperature Qubit Lifetimes of Covalent Organic Frameworks

Zhecheng Sun, Weibin Ni, Denan Li, Xiya Du, Aimei Zhou, Shi Liu, and Lei Sun*

Cite This: J. Am. Chem. Soc. 2025, 147, 31930−31939
Read Online
ACCESS | Metrics & More | Article Recommendations | Supporting Information

ABSTRACT: Molecular electron spin qubits offer atomic-level tunability and room-temperature quantum coherence. Their integration into engineered solid-state matrices can enhance performance toward ambient quantum information technologies. Herein, we demonstrate covalent organic frameworks (COFs) as programmable matrices for stable organic radical qubits, allowing strategic optimization of spin-phonon and spin−spin interactions. Using two classic boronate-ester frameworks, COF-5 and COF-108, to host semiquinone-like radical qubits, we achieve an ultralong spin relaxation time (T_1 > 300 μs) at 298 K, which outperforms most molecular qubits and rivals inorganic spin defects. The suppression of spin relaxation is attributed to rigid and neutral structures as well as carbon-centered spin distributions that effectively weaken spin-phonon coupling. Employing dynamical decoupling methods to both COFs improves their quantum coherence and enables room-temperature detection of nuclear spins, including ^{1}H, ^{11}B, and ^{13}C. Our work establishes COFs as designer quantum materials, opening new avenues for quantum sensing of nuclear spins at room temperature.

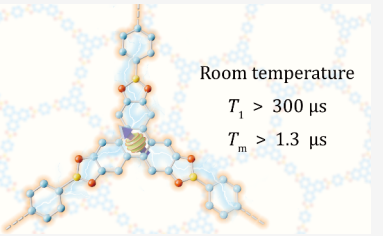

INTRODUCTION

Stable organic radicals, e.g. nitroxide,[1,2] semiquinone,[3,4] triphenylmethyl radicals,[5,6] are molecular electron spin qubits with room temperature quantum coherence. They are promising candidates for ambient quantum information technologies and have enabled prototypical demonstrations of molecular quantum logic gates,[7] quantum sensors,[8] and quantum memories.[9] Incorporating stable organic radicals into metal−organic frameworks (MOFs) and covalent organic frameworks (COFs) facilitates rational optimization of their key qubit metrics including spin relaxation time (T_1) and decoherence time (T_2).[10,11] The corresponding quantum materials, molecular qubit frameworks (MQFs), possess atomically designable, highly ordered, and microporous structures.[12−14] They impart well-defined and fine-tunable spin distributions and phonon dispersion relations, enabling sophisticated control of spin-phonon coupling and spin−spin coupling.[11,15] Their nanoscale pores and functionalizable inner surfaces further facilitate T_1 and T_2 modulations by harnessing host−guest interactions.[16,17] Recent development of MQFs has led to materials with decent room-temperature spin dynamic properties (T_1 = 214 μs, T_2 = 0.98 μs),[18] optically initializable quantum states,[19] and quantum sensing capabilities.[20]

Previously, we investigated two MQFs consisting of HOTP-based semiquinone-like radical qubits (HOTP represents 2,3,6,7,10,11-hexaoxytriphenylene) and diamagnetic metal ions, i.e. $Mg_9(HOTP)_4(H_2O)_{30}$ (MgHOTP) and $[(CH_3)_2NH_2]_2Ti(HOTP)$ (TiHOTP).[11,16,20] The spin relaxation in these frameworks is closely related to their structural rigidity and innate hydrogen bonds. The former determines the density of states (DOS) and cutoff frequencies (Debye frequency, ω_D) of acoustic phonons that drive direct and Raman relaxation processes; the latter affects vibrational modes involving oxygen atoms of HOTP ligands, which stimulate local-mode relaxation processes. Specifically, MgHOTP consists of flexible hydrogen-bonded networks that introduce sub-terahertz optical phonons and expedite spin relaxation. In contrast, the more rigid TiHOTP displays much slower spin relaxation, with T_1 being 41 μs at 294 K. Soaking it in pyridine further improves the structural rigidity and weakens local hydrogen bonds between HOTP and $(CH_3)_2NH_2^+$, enhancing the room-temperature T_1 to 117 μs.

Further improving the T_1 of MQFs necessitates implementing stable organic radicals into more rigid structural motifs. This led us to investigate COF-based MQFs, as covalent bonds (B−O, C═N, etc.) are stronger than coordination bonds and covalent building blocks are typically less flexible than coordination spheres of metal ions.[21,22] Using π-conjugated monomers could promote spin delocalization, which might help protect spins from environmental vibrational and magnetic influences.[23] Moreover, the frameworks can be neutral, leaving no counterions in the pores, and they can be evacuated to remove adsorbed guest molecules.[24] Thus, COFs could provide rigid matrices without innate hydrogen bonds, which combined would improve T_1 and T_2 at room

Received: June 8, 2025
Revised: August 13, 2025
Accepted: August 14, 2025
Published: August 22, 2025

https://doi.org/10.1021/jacs.5c09638
J. Am. Chem. Soc. 2025, 147, 31930−31939

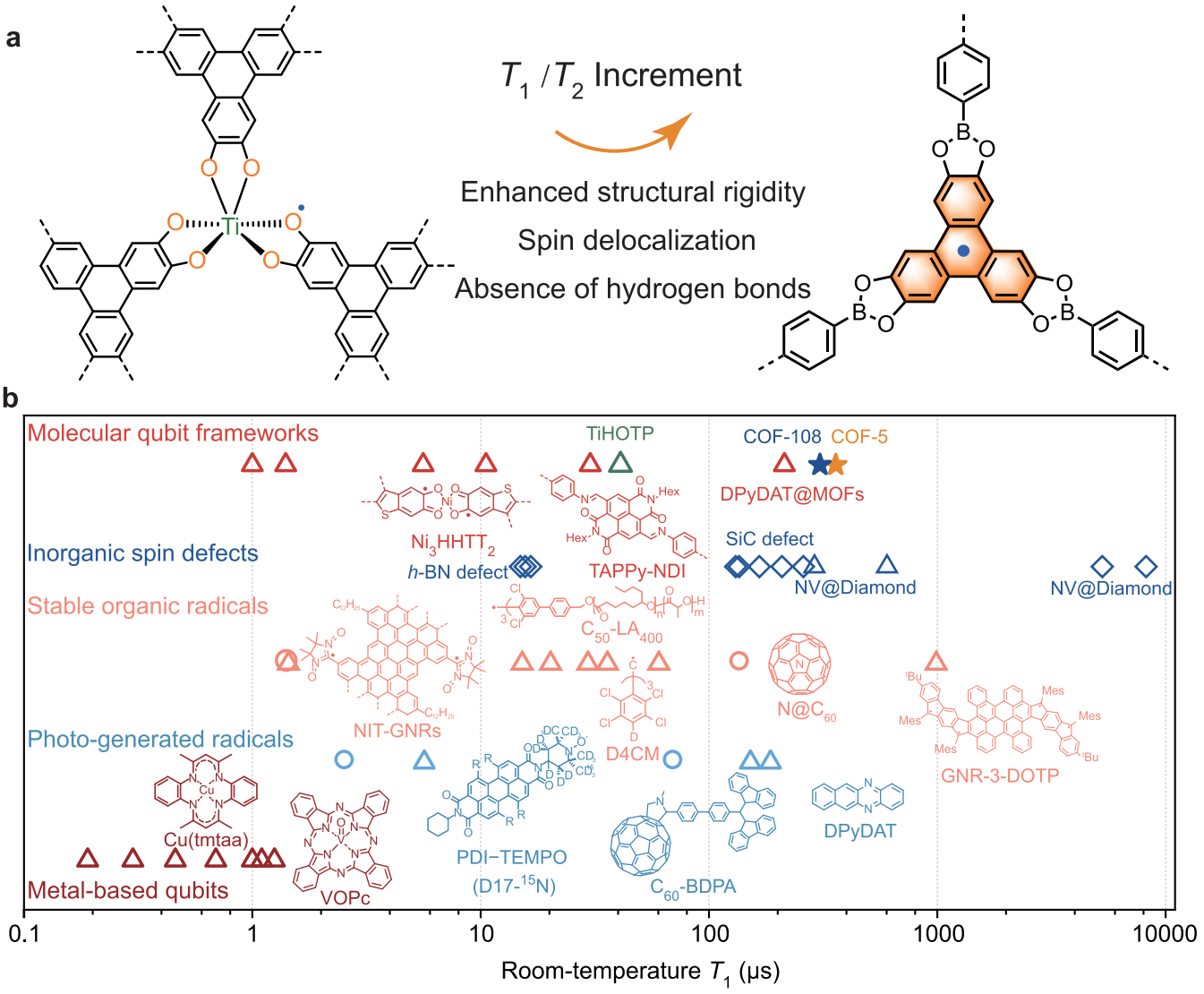

Figure 1. COFs as solid-state hosts for stable organic radical qubits. (a) Advantages of boronate-ester COFs over TiHOTP as MQFs. (b) Comparison of room-temperature T_1 values of COF-5 and COF-108 with those of representative molecular electron spin qubits and paramagnetic defects in dense inorganic solids. Schemes of selected molecules are shown. Full data and the corresponding references are summarized in Table S1. Triangles represent electron spin qubits embedded in solid-state materials or dispersed in solid-state diamagnetic matrices. Circles represent molecular qubits dissolved in fluid solvents. Filled stars represent COF-5 and COF-108. T_1 values of the systems described above were acquired by pulse EPR experiments. Diamonds represent inorganic spin defects whose T_1 values were acquired by optical pumping or optical readout methods.

temperature (Figure 1a). In addition, because their structures can be engineered by rational design of monomers and their spin density can be fine-tuned by postsynthetic modification,[10] COFs enable systematic examination about the influence of structural features, e.g., dimensionality, topology, pore size, etc., and spatial distribution of spins on the qubit performance.[25] Overall, COFs could be excellent solid-state hosts for stable organic radical qubits, yet their potential remains largely unexplored, with only one previous example reported to date exhibiting T_1 and T_2 up to 30.2 and 0.49 μs at 296 K, respectively.[10]

Herein, we report ultralong room-temperature T_1 of HOTP-based qubits embedded in two classic COFs developed by Yaghi et al., namely COF-5 and COF-108.[26,27] These frameworks exhibit T_1 values of 358.0 ± 4.5 μs and 315.1 ± 5.7 μs at 298 K, respectively. They outperform most molecular electron spin qubits at room temperature and are comparable with ensemble paramagnetic defects in dense inorganic solids (Figure 1b). The slow spin relaxation stems from rigid structures, the absence of hydrogen bonds, and carbon-centered spin delocalization as revealed by spin dynamic analysis, specific heat capacity measurements, and density functional theory (DFT) calculations. The long T_1 leads to T_2 reaching 1.3 μs at 298 K, the record for MQFs, and enables room-temperature nuclear spin detection with quantum sensing protocols, showing the potential of radical-integrated COFs for ambient quantum information technologies.[28]

RESULTS AND DISCUSSION

Structures and Phononic Characteristics. We synthesized COF-5 and COF-108 by reacting methylboronic-acid-protected 2,3,6,7,10,11-hexahydroxytriphenylene (HHTP) with pinacol-protected benzene-1,4-diboronic acid (BDBA) or tetra(4-hydroxyborylphenyl) methane (TBPM) based on literature procedures.[27,29] The reversible transesterification reaction between boronic esters helps reduce density of defects

https://doi.org/10.1021/jacs.5c09638
J. Am. Chem. Soc. 2025, 147, 31930−31939

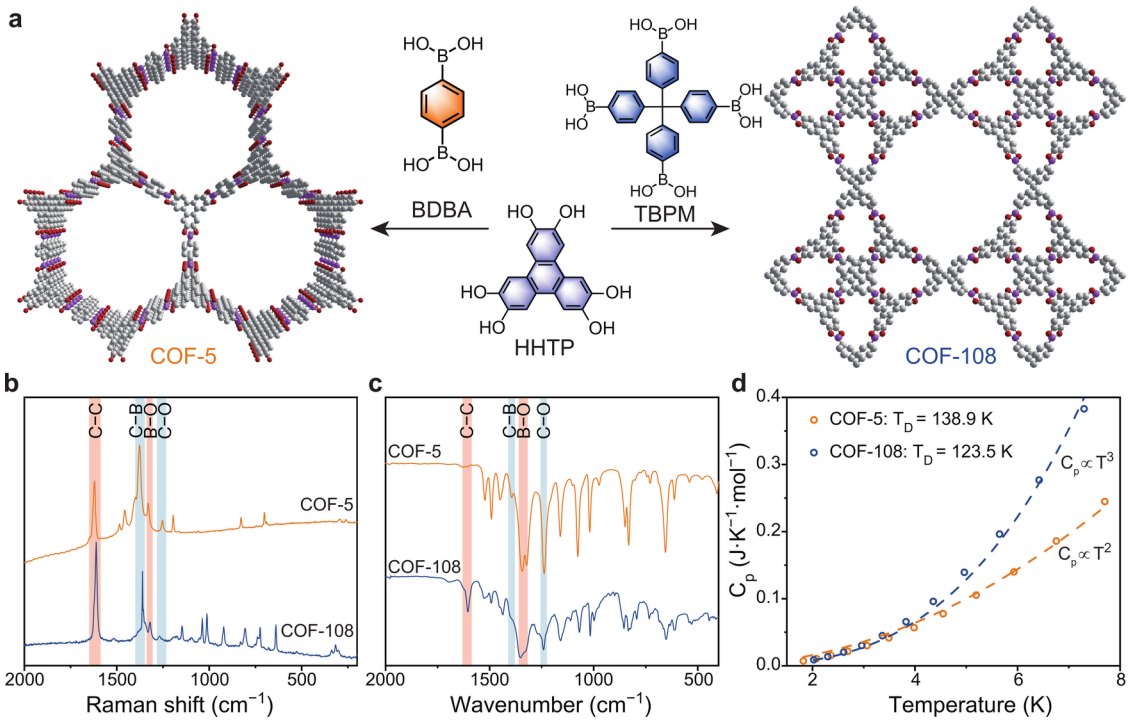

Figure 2. Crystal structures and phonon characteristics. (a) Portions of the crystal structures of COF-5 and COF-108. Gray, purple, and red spheres represent C, B, and O, respectively. H atoms are omitted for clarity. (b) Raman spectra of COF-5 and COF-108 collected at 298 K with 785 and 633 nm excitation, respectively. Stretch modes of representative chemical bonds are highlighted. (c) FT-IR spectra collected at 298 K. (d) Temperature dependencies of specific heat capacity. Circles are experimental data and dash lines are fitting curves.

in the products, thereby improving their crystallinity. Powder X-ray diffraction (PXRD) confirmed structures of target COFs (Figure S1). COF-5 exhibits a 2D layered structure with honeycomb-like planar sheets and eclipsed interlayer stacking (Figure 2a).[26] HOTP moieties form an ordered lamellar architecture facilitated by $\pi-\pi$ interactions. In contrast, COF-108 displays a 3D non-interpenetrated cubic structure nested by triangular HOTP and tetrahedral tetraphenyl methane moieties (Figure 2a).[27] The $\pi-\pi$ interaction is absent between HOTP moieties, as they are spatially separated.

Phonon dispersion relations of COF-5 and COF-108 determine their spin-phonon coupling and in turn spin relaxation processes.[30] Specifically, some optical phonons manifest themselves as vibrations of chemical bonds involving spin-bearing atoms, inducing local-mode relaxation, whose rate is determined by vibrational frequencies. Acoustic phonons could cause direct relaxation by matching electron Zeeman splitting and could participate in Raman relaxation by providing virtual phononic states. The rates of these two processes decrease with the rise of Debye temperature ($T_D = (\hbar\omega_D)/k_B$ where $\hbar$ represents reduced Planck constant and k_B represents Boltzmann constant).

Submicrometer crystal sizes of COF-5 and COF-108 prevented characterization of their complete phonon dispersion relations by inelastic neutron scattering or resonant inelastic X-ray scattering,[27,31] so we conducted Fourier-transform infrared (FT-IR) and Raman spectroscopy to characterize optical phonons at the Gamma point of first Brillouin zone. Both COFs exhibit vibrational peaks at approximately 1250 cm^{-1}, 1330 cm^{-1}, 1377 cm^{-1}, and 1610 cm^{-1} (Figure 2b,c; Figure S2), which are respectively attributed to stretch modes of C−O, B−O, C−B, and C−C bonds.[26,32,33] These high-frequency optical phonons may contribute to local-mode relaxation near room temperature. The lowest-frequency optical phonons of COF-5 and COF-108 are at approximately 260 cm^{-1} and 280 cm^{-1} (Figure 2b,c; Figure S2), respectively, which provide upper limits of T_D as 374 and 403 K.

Experimentally determining T_D helps to reduce the ambiguity of this parameter, providing more accurate insights into spin relaxation mechanisms (*vide infra*). To precisely determine T_D values, we measured specific heat capacity (C_p) of COF-5 and COF-108 at various temperatures (T) (Figure S3a). Both frameworks exhibit low electron spin density (*vide infra*) and behave as electronic insulators (Figure S4), so their C_p dominantly stems from phonons. Below 8 K, C_p values of COF-5 and COF-108 scale with T^2 and T^3, respectively, consistent with Debye models of 2D and 3D systems at the low-temperature limit ($T \ll T_D$):[34−36]

$$\text{2D: } C_p = \frac{24\zeta(3)N_A k_B T^2}{T_D^{\,2}} \tag{1}$$

$$\text{3D: } C_p = \frac{12\pi^4 N_A k_B T^3}{5T_D^{\,3}} \tag{2}$$

where N_A represents Avogadro's number and $\zeta(x)$ is Riemann zeta function. These observations indicate consistent distribution of phonon density of states with structural dimensionality for each COF. Fitting the temperature dependencies of C_p with eqs 1 and 2 revealed T_D values of 138.9 and 123.5 K for COF-5 and COF-108, respectively (Figure 2d). As T_D is a proxy for structural rigidity, COF-5 is slightly more rigid than COF-108 possibly due to the interlayer $\pi-\pi$ stacking in the former. The T_D values of these COFs are higher than that of TiHOTP acquired by the same method (T_D = 110.5 K; Figure

https://doi.org/10.1021/jacs.5c09638
J. Am. Chem. Soc. 2025, 147, 31930−31939

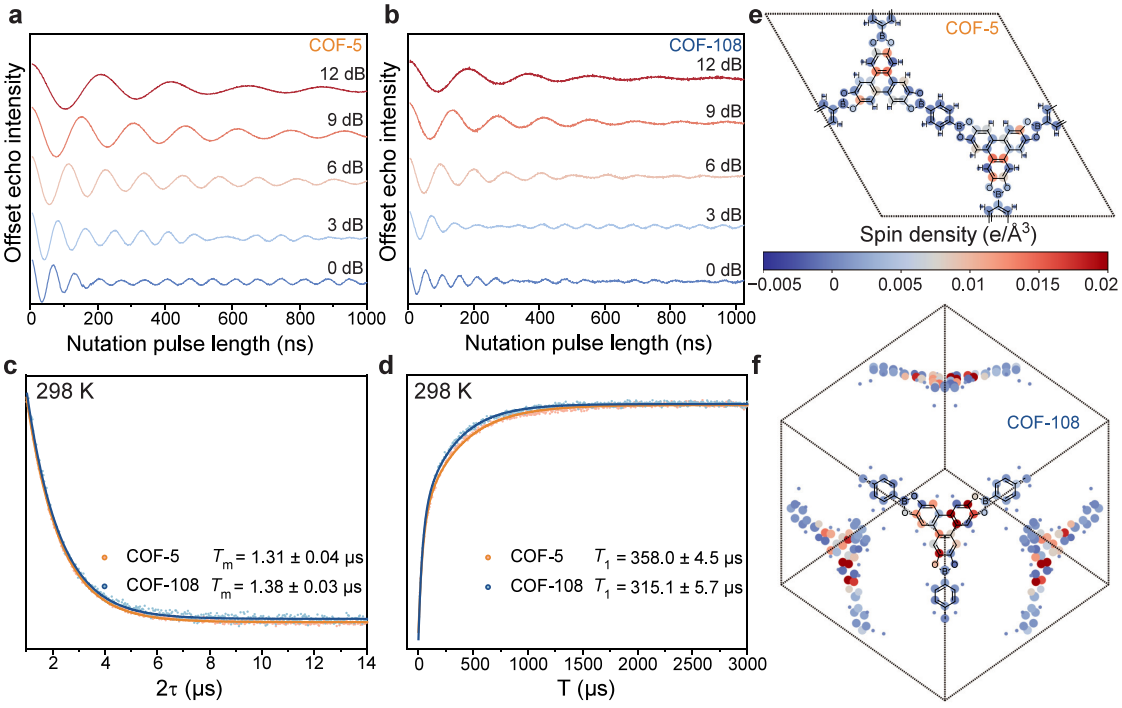

Figure 3. Room-temperature (298 K) qubit performance. (a,b) Rabi oscillations of COF-5 and COF-108. Microwave attenuations are labeled for nutation traces. (c) Hahn echo decay measurements of T_m. Dots are experimental data. Solid lines are monoexponential decay fitting curves. (d) Inversion recovery measurements of T_1. Solid lines are biexponential decay fitting curves. (e,f) Spin density distributions of COF-5 and COF-108.

S3), which is consistent with the larger bond dissociation energy and force constant of B−O bonds compared with those of Ti−O bonds (Figure S7; see detailed discussion in Supporting Information). This reinforces the hypothesis that the boronate ester linker helps improve the structural rigidity of frameworks due to its inherent robustness.

Room-Temperature Qubit Performance. X-band (9.8 GHz) continuous-wave electron paramagnetic resonance (CW-EPR) spectroscopy revealed slight *g*-anisotropy for each framework with COF-5 showing $g_{\parallel}$ = 2.00313 and $g_{\perp}$ = 2.00351 and COF-108 showing $g_{\parallel}$ = 2.00310 and $g_{\perp}$ = 2.00353 (Figure S5a,b). These values are comparable with the free-electron *g*-factor (g_e = 2.00233), confirming the radical characteristics of electron spins. The radical concentrations amount to 5.2 × 10^{14} spins·mm^{-3} (0.019% HOTP) and 9.3 × 10^{14} spins·mm^{-3} (0.048% HOTP) in COF-5 and COF-108, respectively, as indicated by quantitative CW-EPR measurements. Both radical percentages are lower than that of HHTP used for the COF synthesis (0.202% HHTP) (Figure S5c), demonstrating that the transesterification reaction reduces the density of radical defects, i.e. partially oxidized HOTP moieties. DFT calculations show that the electron spin mainly resides on triphenylene moieties in both COFs (Figure 3e,f), exhibiting distinct spin distribution from that of the HOTP radical in MgHOTP and TiHOTP where electron spin is concentrated on oxygen atoms.[11] This difference is likely caused by the electron donation of HOTP to electron-deficient boron, which significantly reduces the electron density on oxygen atoms and leaves the unpaired electron mainly distributed on the aromatic rings. In addition, DFT calculations indicate efficient spin delocalization along the π-stacked HOTP columns in COF-5 (Figure S6), contrasting with localized spin on a single HOTP moiety in COF-108. Thus, comparing these two COFs could reveal the influence of structural dimensionality and its associated spin delocalization among HOTP moieties on the spin dynamics.

We employed X-band pulse EPR spectroscopy to characterize T_1 and phase memory time (T_m), the latter of which encompasses all dephasing factors and represents T_2 for ensemble systems, of COF-5 and COF-108 at room temperature (298 K). We characterized three synthetic batches and conducted six repetitive measurements for a representative batch (discussed below) to confirm reproducibility of T_1 and T_m values (Figure S10 and Table S2). Both COFs exhibited echo-detected field sweep spectra corresponding to S = 1/2 spins (Figure S8) as well as Rabi oscillations in nutation experiments (Figure 3a,b; Figure S9), demonstrating their coherent addressability and qualifying them as MQFs. Their T_m times are 1.31 ± 0.04 μs and 1.38 ± 0.03 μs, respectively, as revealed by Hahn echo decay measurements (Figure 3c; Figure S10 and Table S2), which are longer than the room-temperature T_m of other MQFs (Table S1). Inversion recovery measurements showed comparable behaviors of the two COFs involving two exponential decays. The faster is likely caused by spectral diffusion, whereas the slower is attributed to intrinsic spin relaxation, and its characteristic decay time is assigned to T_1. Remarkably, T_1 times of COF-5 and COF-108 are 358.0 ± 4.5 μs and 315.1 ± 5.7 μs, respectively (Figure 3d; Figure S10 and Table S2). They are significantly longer than the room-temperature value of TiHOTP (T_1 = 41 μs).[11] To our knowledge, these two COFs show comparable T_1 at room temperature with ensemble paramagnetic defects in inorganic solids (e.g., nitrogen−vacancy centers in diamond[37]) and three carbon-centered radicaloids dispersed in *o*-terphenyl,[38] and they outperform all other molecular electron spin qubits encompassing stable organic radicals,[28,39] photo-generated radicals,[40] and coordination complexes[41] (Figure 1b and Table S1).

https://doi.org/10.1021/jacs.5c09638
J. Am. Chem. Soc. 2025, 147, 31930−31939

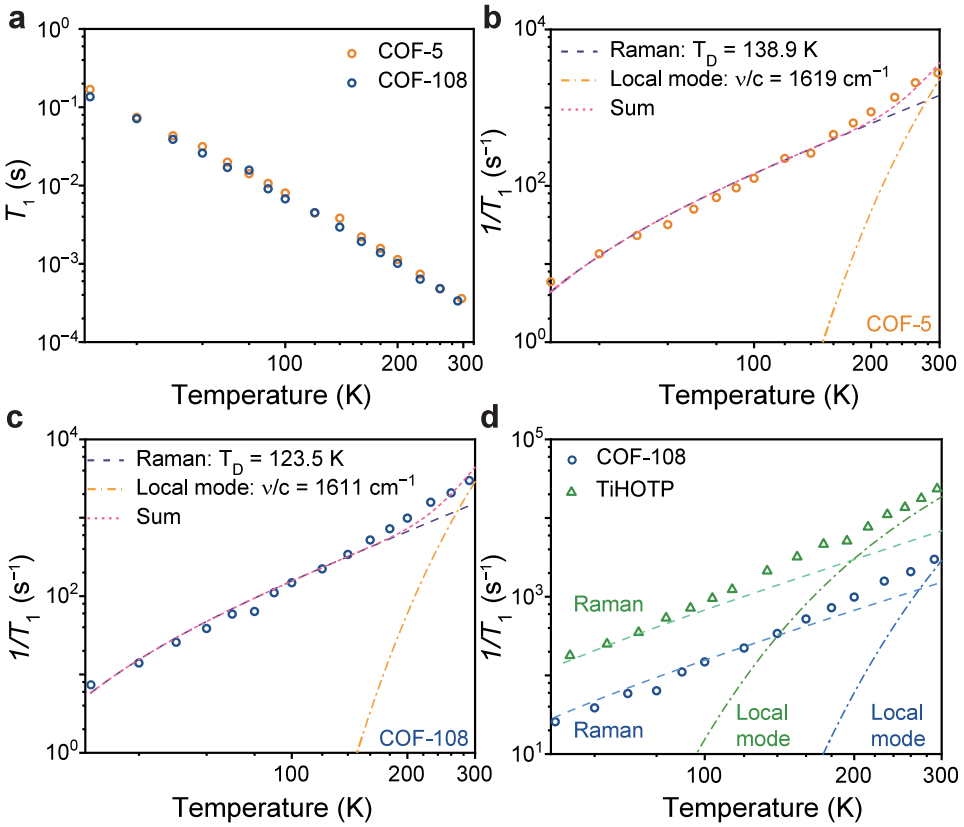

Figure 4. Spin relaxation mechanisms. (a) T_1 of COF-5 and COF-108 acquired at various temperatures. (b,c) Spin relaxation rates ($1/T_1$) acquired at various temperatures and their fitting results. Circles represent the experimental data. Dash lines with various colors represent contributions from individual spin relaxation processes and their sums. Debye temperatures and vibrational frequencies used for fitting are indicated. *c* represents the speed of light. (d) Comparison between the spin relaxation behaviors of COF-108 and TiHOTP. T_1 Data of TiHOTP were extracted from ref 11., and their fitting involves a direct process, an acoustic-phonon-driven Raman process, and a local-mode process induced by Ti−O stretches (ν/c = 714 cm^{-1}) (Figure S12d). Contribution of a direct process was omitted for TiHOTP for the sake of clarity.

Spin Relaxation Mechanisms. To articulate the spin relaxation mechanisms, we measured T_1 of COF-5 and COF-108 in the temperature range of 30−298 K. These two materials exhibited almost identical T_1 at each temperature (Figure 4a), indicating that the structural dimensionality and in turn the spin delocalization among HOTP moieties do not affect spin relaxation. T_1 increases monotonically with decreasing temperature in each COF: it increases from 300−360 μs at 298 K to 130−170 ms at 30 K. It cannot be accurately measured below 30 K due to instrumental limitations (insufficient shot repetition time to recover thermal equilibrium), yet it has the potential to exceed 1 s below 10 K (see Tables S3 and S4). The spin relaxation rate ($1/T_1$) scales with $T^{2.9}$ (Figure S12a), indicating the presence of multiple two-phonon processes driven by both acoustic and optical phonons.[42] As the electron spin density mainly distributes on the triphenylene moieties, both C−C and C−O stretches could induce local-mode relaxation near room temperature.[11] Their contributions are hardly distinguishable due to comparable vibrational frequencies, and involving both modes would cause overfitting (Figure 4b,c; Figure S12b,c and Table S5; see details in the Supporting Information). Hence, we take the local-mode process driven by C−C stretches as an example in the following discussion. In addition, considering the low spin density and relatively high experimental temperatures, both cross relaxation and direct process should be negligible.[11]

Based on this analysis, we fitted the temperature dependence of $1/T_1$ with a Raman process driven by acoustic phonons and a local-mode process driven by C−C stretches:

$$\frac{1}{T_1} = A_{Ram}\left(\frac{T}{T_D}\right)^9 \int_0^{T_D/T} \frac{x^8 e^x}{(e^x - 1)^2} dx + A_{Loc}\frac{e^{h\nu/k_BT}}{(e^{h\nu/k_BT} - 1)^2} \quad (3)$$

where A_{Ram} and A_{Loc} are prefactors of Raman and local-mode processes, respectively, and ν represents the linear frequency of the optical phonon. T_D and ν were extracted from specific heat capacity and vibrational spectroscopic measurements (*vide supra*), respectively, reducing fitting parameters to the two prefactors. This equation yielded decent fitting results (Figure 4b,c; Figure S12e). The Raman relaxation rate scales with T^2 when T approaches or becomes larger than T_D; in contrast, the local-mode relaxation rate increases more sharply with increasing temperature: it follows $\exp(-h\nu/k_BT)$ for $T \ll h\nu/k_B$ ($h\nu/k_B$ > 2300 K for C−C stretches). For both COFs, the Raman process is dominant below 250 K with A_{Ram} being approximately 2 × 10^3 s^{-1}, and the local-mode process dominates above this temperature with A_{Loc} being approximately 6 × 10^6 s^{-1} (Table S5).

For comparison, we re-analyzed spin relaxation mechanisms of TiHOTP using the Debye temperature (T_D = 110.5 K) determined by variable-temperature specific heat capacity measurements (Figure S3b). The analysis revealed the dominant role of the Raman process between 30 and 200 K (Figure S12d). A local-mode process driven by Ti−O stretches

https://doi.org/10.1021/jacs.5c09638
J. Am. Chem. Soc. 2025, 147, 31930−31939

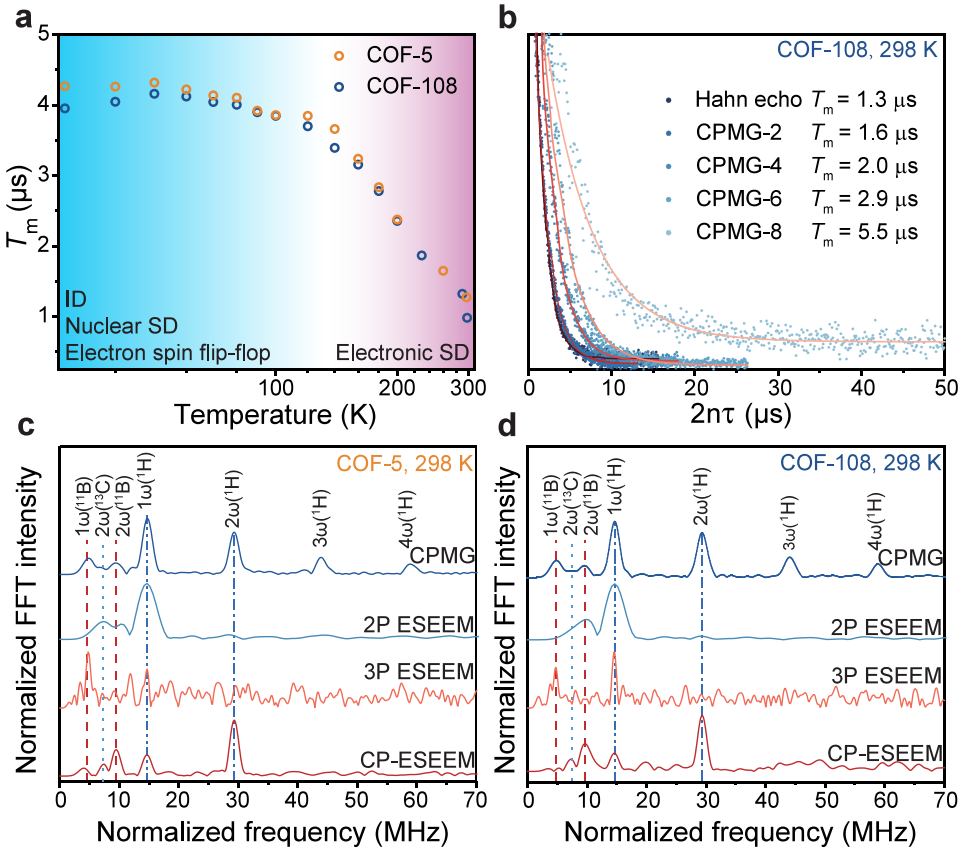

Figure 5. Spin decoherence and nuclear spin modulation. (a) T_m of COF-5 and COF-108 acquired at various temperatures. SD represents spectral diffusion; ID represents instantaneous diffusion. (b) Hahn echo decay and CPMG measurements of T_m at 298 K for COF-108. Circles represent experimental data. Solid lines are monoexponential decay fitting curves. (c,d) Frequency-domain spectra acquired by CPMG-16 and various types of ESEEM sequences at room temperature for COF-5 and COF-108. The n^{th} harmonics of the Larmor frequency of a nuclear spin X are represented as $n\omega(X)$. Frequencies are normalized to $1\omega(^1H)$.

(ν/c = 714 cm^{-1}) dominates above 200 K, which has also been discussed in our previous study.[11] Corresponding A_{Ram} and A_{Loc} are approximately 7.0 × 10^3 s^{-1} and 5.6 × 10^5 s^{-1}, respectively (Table S5).

Both Raman and local-mode relaxation rates of COFs are much slower than those observed for TiHOTP (Figure 4d; see details in the Supporting Information). The suppression of Raman process is likely due to enhanced structural rigidity because B−O bonds and [BO_2C] linkers are more rigid than Ti−O bonds and [TiO_6] coordination spheres, respectively (Figure S7). The local-mode process may be inhibited for three reasons. First, C−C and C−O stretches in COFs exhibit much higher vibrational frequencies than that of the Ti−O stretch in TiHOTP, so the local-mode process in COFs requires higher temperature to activate. Second, the formation of a boronic ester shifts the spin distribution in HOTP from peripheral oxygen atoms to its triphenylene core, making spins less prone to the influence from guest molecules. For instance, soaking COF-5 in a tetrahydrofuran solution of dimethylammonium chloride only reduces its room-temperature T_1 by 12% (Figure S11). This also leads to spin delocalization on triphenylene, which reduces spin density on each atom, so spins are less affected by local vibrations of chemical bonds. Third, both COF-5 and COF-108 are neutral. Evacuating them during sample preparation for pulse EPR measurements could greatly reduce the amount of guest molecules adsorbed in the pores and in turn eliminate local hydrogen bonds involving HOTP. These combined effectively suppress spin relaxation in both COFs, giving rise to the exceptionally long T_1 at room temperature.

Decoherence in COFs and Quantum Sensing Capabilities. We further probed spin decoherence mechanisms of COF-5 and COF-108 by conducting Hahn echo decay measurements from 30 to 298 K (Figure 5a). The T_m values of these two materials are comparable across this temperature range. They remain almost constant below 120 K, indicating that the decoherence is governed by temperature-independent nuclear spectral diffusion, electron spin flip-flop, and/or instantaneous diffusion.[43,44] Above this temperature, T_m drops acutely with the rise of the temperature. Mechanistic analysis revealed the dominant role of electronic spectral diffusion above 120 K for both COFs (Figure S13): spin flip and its diffusion perturb local magnetic environment and accelerates decoherence.[45] In this regime, the decoherence rate is determined by the relaxation rate and spin−spin coupling strength, the latter of which is in turn related to spin density (n): $1/T_m \propto \sqrt{n/T_1}$. Thus, T_1 poses the upper limit for T_m above 120 K even though the former is much longer—the decent T_m values observed at room temperature for both COFs benefit from their exceptionally long T_1. Reducing spin density would further improve the T_m of COFs.[10,43]

We employed a classical dynamical decoupling method, Carr−Purcell−Meiboom−Gill (CPMG) pulse sequence, with a complete phase cycling method to extend T_m at room

https://doi.org/10.1021/jacs.5c09638
J. Am. Chem. Soc. 2025, 147, 31930−31939

temperature.[46,47] The CPMG sequence consists of a series of spin-locking π pulses applied after an initial $\pi/2$ excitation pulse, which refocus the spins and allow for the measurement of spin dynamics over time. This refocusing helps mitigate the effects of inhomogeneous magnetic fields, effectively suppressing the decoherence caused by the electronic and nuclear spectral diffusions. Take COF-108 as an example. Compared with the room-temperature value observed by the Hahn echo decay sequence (T_m = 1.3 μs), applying a CPMG sequence consisting of two π pulses (CPMG-2) improves T_m to 1.6 μs, employing eight π pulses (CPMG-8) extends T_m to 5.5 μs, and using more π pulses does not lead to further improvement likely due to the reduced echo intensity and accumulated pulse errors (Figure 5b and Figure S14b). Applying CPMG-8 to COF-5 improved its T_m from 1.3 to 2.9 μs (Figure S14a). Hence, the T_m of COFs can be improved by dynamically suppressing environmental magnetic noise. Further enhancement of coherence may be achieved by using more robust dynamical decoupling sequences, e.g. XY-8[48] and DROID-60,[49] and at lower temperatures, which demands the sophisticated design of corresponding phase cycling methods.

In addition to prolonging the T_m, the CPMG sequence can also detect alternative-current (AC) magnetic fields. Indeed, employing it to COF-5 and COF-108 generated decay curves with pronounced spectral oscillations (Figure 5b). These oscillations are manifestations of the electron spin echo envelope modulation (ESEEM).[50] They originate from the modulation of electron spin precession in COFs by nuclear spin precession. Under the weak coupling regime where the hyperfine constant is much smaller than the nuclear Larmor frequency, the modulation frequency reflects the gyromagnetic ratio of surrounding nuclear spins, and the modulation depth corresponds to their quantities. As the gyromagnetic ratio is an intrinsic property of a nucleus and differs for different elements and isotopes, it unambiguously reveals the identity of the nucleus. Thus, ESEEM signals can be used to identify and quantify nuclear spins around the electron spin, potentially enabling quantum sensing applications of COF-5 and COF-108.[20]

To further investigate the quantum sensing capability of COFs as well as to articulate environmental nuclear spins that act as decoherence sources, we compared the nuclear spin modulation signals at room temperature obtained from Hahn echo decay (also called 2-pulse (2P) ESEEM), 3-pulse (3P) ESEEM, combination-peak (CP)-ESEEM,[20] and CPMG-16 sequences (Figure S15c).[51] 2P-ESEEM and CPMG sequences leverage electron spin coherence to measure hyperfine interactions, making their resolution fundamentally limited by T_m. In contrast, 3P-ESEEM and CP-ESEEM exploit nuclear spin coherence for hyperfine detection, with their performance being limited by the T_m of nuclear spins and T_1 of the electron spin. Thus, the long T_1 and T_m of COF-5 and COF-108 enable the application of these quantum sensing sequences at room temperature.

Both COFs exhibit clear modulation features from ^{1}H, ^{11}B, and ^{13}C nuclei under these sequences, demonstrating these nuclei as sources of nuclear spectral diffusion (Figure 5c,d; Figure S15a,b). 2P ESEEM generates broad peaks with unresolved low-frequency features, and 3P ESEEM shows weak modulations with a low signal-to-noise ratio (SNR). CPMG-16 gives rise to first to fourth harmonics of ^{1}H, but modulations from ^{11}B and ^{13}C appear as a combined peak, the latter of which are clearly resolved with CP-ESEEM (Figure 5c,d). The observation of ^{11}B at its nuclear Larmor frequency (or second harmonics) indicates negligible hyperfine interaction between HOTP radicals and ^{11}B nuclear spins.[50] This is consistent with the results of DFT calculations: as the electron spin primarily distributes on the conjugated triphenylene moiety, it should interact with ^{11}B nuclei through dipolar coupling rather than Fermi contact, resulting in a weak hyperfine interaction. Overall, these results confirm the capability of COFs for nuclear spin detection and indicate their potential for quantum sensing of nuclear spins, which might empower unambiguous identification and precise quantification of guest molecules.

Comparing the four quantum sensing sequences, we find that increasing the number of π pulses effectively refocuses electron spins, counteracts phase diffusion, and enhances and accumulates periodic modulation signals, thereby significantly improving the SNR for sensing. For the same sample, the CPMG sequence exhibits the strongest modulation depth and the best SNR but has a limited capability to resolve low-frequency signals due to insufficient T_m. In contrast, the CP-ESEEM sequence is effective at resolving low-frequency signals by harnessing the long T_1 but has a limited SNR as a result of its weaker modulation depth. Developing new pulse sequences that integrate the benefits of CPMG and CP-ESEEM holds promise for further improving the sensitivity, spectral resolution, and dynamic range for quantum sensing applications.

CONCLUSIONS AND OUTLOOK

In conclusion, COF-5 and COF-108 exhibit excellent qubit performance at room temperature. The rigid structures, triphenylene-centered spin distributions, and absence of hydrogen bonds in these two frameworks together suppress spin relaxation. This leads to T_1 above 300 μs at 298 K, which is longer than the values observed for most molecular electron spin qubits. The ultralong T_1 gives rise to T_m reaching 1.3 μs at room temperature, setting a record for MQFs. The excellent qubit performance enables applications of dynamical decoupling and ESEEM sequences, showing the capability of COF-5 and COF-108 for nuclear spin detection. The foregoing results demonstrate that COFs provide viable solid-state hosts for molecular electron spin qubits. Integrating design principles unveiled in this study with well-established synthetic methodologies for radical-embedded COFs could lead to MQFs with long T_1 and T_m at room temperature.[52−54] Rational design and post-synthetic modification of the inner surfaces of COFs would further generate candidate materials for quantum sensing of nuclear spins in ambient conditions.

ASSOCIATED CONTENT

Supporting Information

The Supporting Information is available free of charge at https://pubs.acs.org/doi/10.1021/jacs.5c09638.

PXRD patterns, IR spectra, specific heat capacity characterization results, electrical characterization results, EPR characterization results, DFT calculation results, and spin dynamics of room-temperature electron spin qubits as well as their associated references. (PDF)

https://doi.org/10.1021/jacs.5c09638
J. Am. Chem. Soc. 2025, 147, 31930−31939

AUTHOR INFORMATION

Corresponding Author

Lei Sun − *Department of Chemistry, School of Science and Research Center for Industries of the Future, Westlake University, Hangzhou 310030 Zhejiang Province, China; Institute of Natural Sciences, Westlake Institute for Advanced Study, Hangzhou 310024 Zhejiang Province, China; Department of Physics, School of Science and Research Center for Industries of the Future, Westlake University, Hangzhou 310030 Zhejiang Province, China;* orcid.org/0000-0001-8467-6750; Email: sunlei@westlake.edu.cn

Authors

Zhecheng Sun − *Department of Chemistry, School of Science and Research Center for Industries of the Future, Westlake University, Hangzhou 310030 Zhejiang Province, China; Institute of Natural Sciences, Westlake Institute for Advanced Study, Hangzhou 310024 Zhejiang Province, China;* orcid.org/0000-0003-0786-3514

Weibin Ni − *Institute of Natural Sciences, Westlake Institute for Advanced Study, Hangzhou 310024 Zhejiang Province, China; Department of Physics, School of Science and Research Center for Industries of the Future, Westlake University, Hangzhou 310030 Zhejiang Province, China*

Denan Li − *Department of Physics, School of Science and Research Center for Industries of the Future, Westlake University, Hangzhou 310030 Zhejiang Province, China*

Xiya Du − *Department of Chemistry, School of Science and Research Center for Industries of the Future, Westlake University, Hangzhou 310030 Zhejiang Province, China; Institute of Natural Sciences, Westlake Institute for Advanced Study, Hangzhou 310024 Zhejiang Province, China;* orcid.org/0009-0000-3687-1009

Aimei Zhou − *Department of Chemistry, School of Science and Research Center for Industries of the Future, Westlake University, Hangzhou 310030 Zhejiang Province, China; Institute of Natural Sciences, Westlake Institute for Advanced Study, Hangzhou 310024 Zhejiang Province, China*

Shi Liu − *Department of Chemistry, School of Science and Research Center for Industries of the Future, Westlake University, Hangzhou 310030 Zhejiang Province, China; Institute of Natural Sciences, Westlake Institute for Advanced Study, Hangzhou 310024 Zhejiang Province, China; Department of Physics, School of Science and Research Center for Industries of the Future, Westlake University, Hangzhou 310030 Zhejiang Province, China;* orcid.org/0000-0002-8488-4848

Complete contact information is available at: https://pubs.acs.org/10.1021/jacs.5c09638

Notes

The authors declare no competing financial interest.

ACKNOWLEDGMENTS

This work was supported by the National Natural Science Foundation of China (Grant No. 22273078) and the Hangzhou Municipal Innovation Team Program (TD2022004). S.L. acknowledges the support from Zhejiang Provincial Natural Science Foundation of China (LR25A040004). We are grateful to Dr. Zhongyue Zhang for valuable discussions. Z.S. acknowledges Danyu Gu and Dr. Shutian Lu for assistance with EPR spectroscopy, Dr. Shaoze Wang and Dr. Chao Zhang for assistance with specific heat capacity measurements and data analysis, Jufang Zheng for assistance with far-IR spectroscopy, and Haoming Ren for assistance in artistic design. Z.S. and L.S. thank the Instrumentation and Service Center for Molecular Sciences and the Instrumentation and Service Center for Physical Sciences at Westlake University for providing facility access and technical support. Computational resources were provided by the Westlake HPC Center.

REFERENCES

(1) Kuzhelev, A. A.; Strizhakov, R. K.; Krumkacheva, O. A.; Polienko, Y. F.; Morozov, D. A.; Shevelev, G. Yu; Pyshnyi, D. V.; Kirilyuk, I. A.; Fedin, M. V.; Bagryanskaya, E. G. Room-Temperature Electron Spin Relaxation of Nitroxides Immobilized in Trehalose: Effect of Substituents Adjacent to NO-Group. *J. Magn. Reson.* **2016**, *266*, 1−7.

(2) Sato, H.; Bottle, S. E.; Blinco, J. P.; Micallef, A. S.; Eaton, G. R.; Eaton, S. S. Electron Spin-Lattice Relaxation of Nitroxyl Radicals in Temperature Ranges That Span Glassy Solutions to Low-Viscosity Liquids. *J. Magn. Reson.* **2008**, *191*, 66−77.

(3) Kathirvelu, V.; Sato, H.; Eaton, S. S.; Eaton, G. R. Electron Spin Relaxation Rates for Semiquinones between 25 and 295K in Glass-Forming Solvents. *J. Magn. Reson.* **2009**, *198*, 111−120.

(4) Elajaili, H. B.; Biller, J. R.; Eaton, S. S.; Eaton, G. R. Frequency Dependence of Electron Spin-Lattice Relaxation for Semiquinones in Alcohol Solutions. *J. Magn. Reson.* **2014**, *247*, 81−87.

(5) Yong, L.; Harbridge, J.; Quine, R. W.; Rinard, G. A.; Eaton, S. S.; Eaton, G. R.; Mailer, C.; Barth, E.; Halpern, H. J. Electron Spin Relaxation of Triarylmethyl Radicals in Fluid Solution. *J. Magn. Reson.* **2001**, *152*, 156−161.

(6) Dai, Y.; Dong, B.; Kao, Y.; Wang, Z.; Un, H.; Liu, Z.; Lin, Z.; Li, L.; Xie, F.; Lu, Y.; Xu, M.; Lei, T.; Sun, Y.; Wang, J.; Gao, S.; Jiang, S.; Pei, J. Chemical Modification toward Long Spin Lifetimes in Organic Conjugated Radicals. *ChemPhysChem* **2018**, *19*, 2972−2977.

(7) Nakazawa, S.; Nishida, S.; Ise, T.; Yoshino, T.; Mori, N.; Rahimi, R. D.; Sato, K.; Morita, Y.; Toyota, K.; Shiomi, D.; Kitagawa, M.; Hara, H.; Carl, P.; Höfer, P.; Takui, T. A Synthetic Two-spin Quantum Bit: G-engineered Exchange-coupled Biradical Designed for Controlled-NOT Gate Operations. *Angew. Chem., Int. Ed.* **2012**, *51*, 9860−9864.

(8) Bonizzoni, C.; Ghirri, A.; Santanni, F.; Affronte, M. Quantum Sensing of Magnetic Fields with Molecular Spins. *npj Quantum Inf.* **2024**, *10*, 41.

(9) Lenz, S.; Konig, D.; Hunger, D.; van Slageren, J. Room-Temperature Quantum Memories Based on Molecular Electron Spin Ensembles. *Adv. Mater.* **2021**, *33*, 2101673.

(10) Oanta, A. K.; Collins, K. A.; Evans, A. M.; Pratik, S. M.; Hall, L. A.; Strauss, M. J.; Marder, S. R.; D'Alessandro, D. M.; Rajh, T.; Freedman, D. E.; Li, H.; Brédas, J.-L.; Sun, L.; Dichtel, W. R. Electronic Spin Qubit Candidates Arrayed within Layered Two-Dimensional Polymers. *J. Am. Chem. Soc.* **2023**, *145*, 689−696.

(11) Zhou, A.; Li, D.; Tan, M.; Lv, Y.; Pang, S.; Zhao, X.; Shi, Z.; Zhang, J.; Jin, F.; Liu, S.; Sun, L. Phononic Modulation of Spin-Lattice Relaxation in Molecular Qubit Frameworks. *Nat. Commun.* **2024**, *15*, 10763.

(12) Tomilov, A. S.; Yazikova, A. A.; Melnikov, A. R.; Smirnova, K. A.; Poryvaev, A. S.; Fedin, M. V. Scalable Approach for Grafting Qubit Candidates onto the Surface of MOF-808 Framework. *Russ. J. Coord. Chem.* **2024**, *50*, 646−652.

(13) Lu, Y.; Hu, Z.; Petkov, P.; Fu, S.; Qi, H.; Huang, C.; Liu, Y.; Huang, X.; Wang, M.; Zhang, P.; Kaiser, U.; Bonn, M.; Wang, H. I.; Samorì, P.; Coronado, E.; Dong, R.; Feng, X. Tunable Charge Transport and Spin Dynamics in Two-Dimensional Conjugated Meta-Organic Frameworks. *J. Am. Chem. Soc.* **2024**, *146*, 2574−2582.

(14) Lu, Y.; Fu, Y.; Hu, Z.; Feng, S.; Torabi, M.; Gao, L.; Fu, S.; Wang, Z.; Huang, C.; Huang, X.; Wang, M.; Israel, N.; Dmitrieva, E.; Wang, H. I.; Bonn, M.; Samorì, P.; Dong, R.; Coronado, E.; Feng, X.

Rational Construction of Layered Two-Dimensional Conjugated Metal-Organic Frameworks with Room-Temperature Quantum Coherence. *J. Am. Chem. Soc.* **2025**, *147*, 8778−8784.
(15) Yu, C.-J.; von Kugelgen, S.; Krzyaniak, M. D.; Ji, W.; Dichtel, W. R.; Wasielewski, M. R.; Freedman, D. E. Spin and Phonon Design in Modular Arrays of Molecular Qubits. *Chem. Mater.* **2020**, *32*, 10200−10206.
(16) Zhou, A.; Sun, L. Quantum Sensing of Microscopic Viscosity with a Molecular Qubit Framework. *APL Mater.* **2025**, *13*, 031120.
(17) Inoue, M.; Yamauchi, A.; Parmar, B.; Orihashi, K.; Singh, M.; Asada, M.; Nakamura, T.; Yanai, N. Guest-Responsive Coherence Time of Radical Qubits in a Metal-Organic Framework. *Chem. Commun.* **2024**, *60*, 6130−6133.
(18) Orihashi, K.; Yamauchi, A.; Fujiwara, S.; Asada, M.; Nakamura, T.; Ka-Ho Hui, J.; Kimizuka, N.; Tateishi, K.; Uesaka, T.; Yanai, N. Spin-Polarized Radicals with Extremely Long Spin-Lattice Relaxation Time at Room Temperature in a Metal-Organic Framework. *J. Am. Chem. Soc.* **2023**, *145*, 27650−27656.
(19) Yamauchi, A.; Tanaka, K.; Fuki, M.; Fujiwara, S.; Kimizuka, N.; Ryu, T.; Saigo, M.; Onda, K.; Kusumoto, R.; Ueno, N.; Sato, H.; Kobori, Y.; Miyata, K.; Yanai, N. Room-Temperature Quantum Coherence of Entangled Multiexcitons in a Metal-Organic Framework. *Sci. Adv.* **2024**, *10*, No. eadi3147.
(20) Sun, L.; Yang, L.; Dou, J.-H.; Li, J.; Skorupskii, G.; Mardini, M.; Tan, K. O.; Chen, T.; Sun, C.; Oppenheim, J. J.; Griffin, R. G.; Dincă, M.; Rajh, T. Room-Temperature Quantitative Quantum Sensing of Lithium Ions with a Radical-Embedded Metal-Organic Framework. *J. Am. Chem. Soc.* **2022**, *144*, 19008−19016.
(21) Liu, R.; Tan, K. T.; Gong, Y.; Chen, Y.; Li, Z.; Xie, S.; He, T.; Lu, Z.; Yang, H.; Jiang, D. Covalent Organic Frameworks: An Ideal Platform for Designing Ordered Materials and Advanced Applications. *Chem. Soc. Rev.* **2021**, *50*, 120−242.
(22) Yaghi, O. M.; Kalmutzki, M. J.; Diercks, C. S. *Introduction to Reticular Chemistry*; Wiley-VCH: 2019; pp 225−243.
(23) Dougherty, D. A Spin Control in Organic Molecules. *Acc. Chem. Res.* **1991**, *24*, 88−94.
(24) Zhu, D.; Verduzco, R. Ultralow Surface Tension Solvents Enable Facile COF Activation with Reduced Pore Collapse. *ACS Appl. Mater. Interfaces* **2020**, *12*, 33121−33127.
(25) Tan, K. T.; Ghosh, S.; Wang, Z.; Wen, F.; Rodríguez-San-Miguel, D.; Feng, J.; Huang, N.; Wang, W.; Zamora, F.; Feng, X.; Thomas, A.; Jiang, D. Covalent Organic Frameworks. *Nat. Rev. Methods Prim.* **2023**, *3*, 1−19.
(26) Côté, A. P.; Benin, A. I.; Ockwig, N. W.; O'Keeffe, M.; Matzger, A. J.; Yaghi, O. M. Porous, Crystalline, Covalent Organic Frameworks. *Science* **2005**, *310*, 1166−1170.
(27) El-Kaderi, H. M.; Hunt, J. R.; Mendoza-Cortés, J. L.; Côté, A. P.; Taylor, R. E.; O'Keeffe, M.; Yaghi, O. M. Designed Synthesis of 3D Covalent Organic Frameworks. *Science* **2007**, *316*, 268−272.
(28) Zhou, A.; Sun, Z.; Sun, L. Stable Organic Radical Qubits and Their Applications in Quantum Information Science. *Innovation* **2024**, *5*, 100662.
(29) Hamzehpoor, E.; Jonderian, A.; McCalla, E.; Perepichka, D. F. Synthesis of Boroxine and Dioxaborole Covalent Organic Frameworks via Transesterification and Metathesis of Pinacol Boronates. *J. Am. Chem. Soc.* **2021**, *143*, 13274−13280.
(30) Eaton, S. S.; Eaton, G. R. Realxation Times. *eMagRes.* **2019**, *5*, 1543−1556.
(31) Evans, A. M.; Parent, L. R.; Flanders, N. C.; Bisbey, R. P.; Vitaku, E.; Kirschner, M. S.; Schaller, R. D.; Chen, L. X.; Gianneschi, N. C.; Dichtel, W. R. Seeded Growth of Single-Crystal Two-Dimensional Covalent Organic Frameworks. *Science* **2018**, *361*, 52−57.
(32) Sun, J.; Iakunkov, A.; Baburin, I. A.; Joseph, B.; Palermo, V.; Talyzin, A. V. Covalent Organic Framework (COF-1) under High Pressure. *Angew. Chem., Int. Ed.* **2020**, *59*, 1087−1092.
(33) Liu, Z.; Su, R.; Xiao, X.; Li, G. Boronic Acid Ester-Based Hydrogel as Surface-Enhanced Raman Scattering Substrates for Separation, Enrichment, Hydrolysis and Detection of Hydrogen Peroxide Residue in Dairy Product All-in-One. *Talanta* **2025**, *281*, 126900.
(34) Krumhansl, J.; Brooks, H. The Lattice Vibration Specific Heat of Graphite. *J. Chem. Phys.* **1953**, *21*, 1663−1669.
(35) Sichel, E. K.; Miller, R. E.; Abrahams, M. S.; Buiocchi, C. J. Heat Capacity and Thermal Conductivity of Hexagonal Pyrolytic Boron Nitride. *Phys. Rev. B* **1976**, *13*, 4607−4611.
(36) Debye, P. Zur Theorie Der Spezifischen Wärmen. *Ann. Phys.* **1912**, *344*, 789−839.
(37) Peng, Z.; Dallas, J.; Takahashi, S. Reduction of Surface Spin-Induced Electron Spin Relaxations in Nanodiamonds. *J. Appl. Phys.* **2020**, *128*, 054301.
(38) Lombardi, F.; Ma, J.; Alexandropoulos, D. I.; Komber, H.; Liu, J.; Myers, W. K.; Feng, X.; Bogani, L. Synthetic Tuning of the Quantum Properties of Open-Shell Radicaloids. *Chem.* **2021**, *7*, 1363−1378.
(39) Hou, L.; Zhang, Y.; Zhang, Y.; Jiang, S.; Wang, M. Tunable Quantum Coherence of Luminescent Molecular Spins Organized via Block Copolymer Self-Assembly. *Adv. Quantum Technol.* **2024**, *7*, 2400064.
(40) Orihashi, K.; Yamauchi, A.; Inoue, M.; Parmar, B.; Fujiwara, S.; Kimizuka, N.; Asada, M.; Nakamura, T.; Yanai, N. Radical Qubits Photo-Generated in Acene-Based Metal-Organic Frameworks. *Dalton Trans.* **2024**, *53*, 872−876.
(41) Mullin, K. R.; Johnson, D.; Freedman, D. E.; Rondinelli, J. M. Systems-Chart Approach to the Design of Spin Relaxation Times in Molecular Qubits. *Dalton Trans.* **2024**, *53*, 16585−16591.
(42) Gu, L.; Wu, R. Origin of the Anomalously Low Raman Exponents in Single Molecule Magnets. *Phys. Rev. B* **2021**, *103*, 014401.
(43) Du, X.; Sun, L. Optimizing the Spin Qubit Performance of Lanthanide-Based Metal-Organic Frameworks. *Inorg. Chem. Front.* **2024**, *11*, 8660−8670.
(44) Wilson, C. B.; Qi, M.; Han, S.; Sherwin, M. S. Gadolinium Spin Decoherence Mechanisms at High Magnetic Fields. *J. Phys. Chem. Lett.* **2023**, *14*, 10578−10584.
(45) Lim, H.-J.; Welinski, S.; Ferrier, A.; Goldner, P.; Morton, J. J. L. Coherent Spin Dynamics of Ytterbium Ions in Yttrium Orthosilicate. *Phys. Rev. B* **2018**, *97*, 064409.
(46) Du, J.; Rong, X.; Zhao, N.; Wang, Y.; Yang, J.; Liu, R. B. Preserving Electron Spin Coherence in Solids by Optimal Dynamical Decoupling. *Nature* **2009**, *461*, 1265−1268.
(47) Lombardi, F.; Myers, W. K.; Ma, J.; Liu, J.; Feng, X.; Bogani, L. Dynamical Nuclear Decoupling of Electron Spins in Molecular Graphenoid Radicals and Biradicals. *Phys. Rev. B* **2020**, *101*, 094406.
(48) Gullion, T.; Baker, D. B.; Conradi, M. S. New, Compensated Carr-Purcell Sequences. *J. Magn. Reson.* **1990**, *89*, 479−484.
(49) Choi, J.; Zhou, H.; Knowles, H. S.; Landig, R.; Choi, S.; Lukin, M. D. Robust Dynamic Hamiltonian Engineering of Many-Body Spin Systems. *Phys. Rev. X* **2020**, *10*, 031002.
(50) Doorslaer, S. V. Hyperfine Spectroscopy - ESEEM. In *EPR Spectroscopy: Fundamentals and Methods*; Goldfarb, D., Stoll, S., Eds.; John Wiley & Sons: 2018; pp 377−400.
(51) Mitrikas, G.; Prokopiou, G. Modulation Depth Enhancement of ESEEM Experiments Using Pulse Trains. *J. Magn. Reson.* **2015**, *254*, 75−85.
(52) Cao, W.; Wang, W. D.; Xu, H.-S.; Sergeyev, I. V.; Struppe, J.; Wang, X.; Mentink-Vigier, F.; Gan, Z.; Xiao, M.-X.; Wang, L.-Y.; Chen, G.-P.; Ding, S.-Y.; Bai, S.; Wang, W. Exploring Applications of Covalent Organic Frameworks: Homogeneous Reticulation of Radicals for Dynamic Nuclear Polarization. *J. Am. Chem. Soc.* **2018**, *140*, 6969−6977.
(53) Wu, S.; Li, M.; Phan, H.; Wang, D.; Herng, T. S.; Ding, J.; Lu, Z.; Wu, J. Toward Two-Dimensional π-Conjugated Covalent Organic Radical Frameworks. *Angew. Chem., Int. Ed.* **2018**, *57*, 8007−8011.
(54) Su, X.; Cheng, L.; Yan, X.; Zhang, H.; Wang, T.; Wang, H.-G.; Chen, L. In Situ Construction of Amide-Functionalized 2D Conjugated Metal-Organic Frameworks with Multiple Active Sites

for High-Performance Potassium-Ion Batteries. *J. Am. Chem. Soc.* **2025**, *147*, 18338−18348.

https://doi.org/10.1021/jacs.5c09638
J. Am. Chem. Soc. 2025, 147, 31930−31939